Journal of Computational Physics 392 (2019) 578–593

Contents lists available at ScienceDirect

Journal of Computational Physics

www.elsevier.com/locate/jcp

An image-guided computational approach to inversely determine *in vivo* material properties and model flow-structure interactions of fish fins

Geng Liu [a,1], Biao Geng [a,1], Xudong Zheng [a], Qian Xue [a,*], Haibo Dong [b], George V. Lauder [c]

[a] Department of Mechanical Engineering, University of Maine, Orono, ME 04469, USA
[b] Department of Mechanical and Aerospace Engineering, University of Virginia, Charlottesville, VA 22904, USA
[c] Department of Organismic and Evolutionary Biology, Harvard University, Cambridge, MA 02138, USA

ARTICLE INFO

Article history:
Received 13 August 2018
Received in revised form 5 March 2019
Accepted 26 April 2019
Available online 3 May 2019

Keywords:
Fish swimming
Flexible fin
Flow-structure interaction
Optimization

ABSTRACT

We present an image-guided computational approach for inversely determining *in vivo* material properties of fish fins and simulating flow-structure interactions (FSI) of fin deformations based on a highly realistic hybrid membrane-beam structure. This approach is established by coupling an imaged-based reconstruction, a genetic-algorithm (GA)-based optimization, a finite-element-method (FEM)-based computational structural dynamics model and an immersed-boundary-method (IBM)-based computational fluid dynamics (CFD) solver. An inverse-problem procedure is developed to determine material properties from prescribed kinematic motions obtained from high-speed images. The procedure is validated through two tests including a flexible pitching plate and a shell-beam structured flexible plate in heaving motion. The FSI model (forward problem) is validated through two benchmark tests including flow-induced vibration of a flexible beam attached to a fixed cylinder and a flexible pitching plate in a uniform flow. This integrated method is then applied to the FSI analysis of propulsion of a rainbow trout caudal fin with a specific focus on the fin material properties, fin deformations, hydrodynamic performances and flow structures. We demonstrate that, by using reconstructed kinematics and deformation obtained from the high-speed videos, the non-uniform material properties of the fin can be determined through the inverse problem procedure. A fully-coupled FSI simulation is then carried out based on the outcome of the inverse problem. The results have shown the feasibility of the present integrated approach in accurately modeling and quantitatively evaluating flexible-fin kinematics and hydrodynamics in swimming in terms of both chordwise and spanwise deformations, thrust and lateral forces, and vortex dynamics.

1. Introduction

Fish fin is an important biological model for designing novel underwater propulsors. Extensive research effort has been devoted to understanding the interactions between fish fins and flows as well as their effect on propulsion performance [1–8]. In particular, the formation mechanism as well as the functional role of the special deforming modes of fish fins in

* Corresponding author.
E-mail address: qian.xue@maine.edu (Q. Xue).
[1] Both authors have contributed equally.

https://doi.org/10.1016/j.jcp.2019.04.062
0021-9991/

propulsion have been of great interests to both the researchers and the designers because they have been demonstrated to significantly improve the hydrodynamic performance [6,8–12].

The special deforming modes are the outcome of the flow-structure interactions of fish fins and are thought to be associated with the complex structural configuration and material properties. Fish fins usually consist of a series of bony rays and a pliable membrane supported by those rays. The flexural stiffness of a fin is primarily attributed to the rays. But the rays are not simple structures, either. Each ray is tapered and branches as it approach the trailing edge of a fin [13]. Also, the fin ray structures display a varying configuration along the length. For example, a ray from a bluegill sunfish pectoral fin shows that the proximal portion is unsegmented while the distal 60% of the fin ray is segmented [14]. Moreover, the compositions of biomaterials are also non-uniformly distributed along each ray and among rays [15,16]. These features contribute to a non-uniformly distributed stiffness pattern on fish fin. This non-uniform stiffness pattern along with the non-homogeneous density distribution resulted from the complex anatomical structures pose challenges on numerical modeling and bio-inspired man-made design.

Computational modeling of the flow-structure interaction in fish fin propulsion is challenging due to the aforementioned complex anatomical structures, non-uniform material properties and strong coupling between flow and structure. Past studies predominantly relied on simplified structures, materials or physics. For example, many studies simplified the fin structure into a rigid plate/foil [17,18] or flexible ones with uniform flexibility in the chordwise and/or spanwise direction [6,19–23]. Some models employed a prescribed fin kinematics, which was either reconstructed from high-speed videos [24,25] or mathematically specified [26,27], by just focusing on the hydrodynamic response of the deformation. Recently, a number of higher-fidelity models were developed. Considering that most fish fins are soft collagenous membranes supported by a series of bony fin rays, Zhu and Shoele [6] built a spring-connected-rays model of a fish caudal fin and coupled it with a boundary-element-method-based potential flow solver to achieve FSI simulations. The model was used to study the effect of anisotropic deformability of fish fin due to non-uniform distributions of fin rays on fin propulsion. It was found that the anisotropic deformability can significantly improve thrust generation and propulsive efficiency in a dorsal-ventrally symmetric flapping motion. This type of spring-connected ray structure has also been applied to model fish pectoral fins [7,28]. Similar hybrid membrane-beam structural models were also employed for studying other biological propulsors (fins/wings) [20,29,30]. Despite the advances in modeling the realistic hybrid membrane-beam structure of the fins, these studies were still limited to simple deformability by using constant stiffness throughout the fin or fin rays. Without the realistic stiffness pattern, FSI simulations will be unable to reproduce the realistic fin morphology and kinematics.

The stiffness patterns of fish fins were previously studied by *in vitro* measurements [16]. The results confirmed that flexural stiffness varies along each fin ray and among rays. However, these *in vitro* measurements were usually only on selective rays. Also, the actual stiffness pattern during active swimming could be very different from *in vitro* measurements. To get a more accurate stiffness pattern of flapping fish fins, image-based inverse determination of *in vivo* material properties will be employed in this paper. This method is an optimization framework based on a finite element method (FEM) and high-speed images. Given the desired output surface (acquired by reconstruction), during the optimization, the input model is deformed by the FEM simulator according to the guessed elasticity parameters. And the guessed elasticity parameters are thought to be the correct values when an objective function based on the distance between the deformed surface and the desired surface is minimum. This optimization framework does not depend on a particular simulation method or data acquisition and is therefore suitable for different physical problems, such as biomedical researches for the estimation of elasticity parameters in live organs or cancerous tissues [31–33]. However, in most biomedical applications, there is no such fluid flow involved (and therefore no FSI) as that in the fish fin propulsion problem.

In this study, we present an integrated approach for modeling the *in vivo* material properties of fish fins and the FSI in flapping propulsion, which combines a high-speed photogrammetry, direct measurement of fin kinematics and deformation based on a high-fidelity 3D model reconstruction, a FEM analysis of the hybrid membrane-beam structure, a genetic algorithm-based optimization, and a CFD solver. The material properties of fin membrane and each fin ray are inversely predicted by the optimization based on the FEM analysis and the reconstruction. With the resulting predicted fin ray stiffness pattern and a fully coupled FSI solver, we are able to reproduce the fin kinematics with good quantitative agreement with high-speed videos. The interplay between structure, kinematics and fluid flow of a fish fin are also studied. The content of this paper is structured as follows. In section 2, the method of inverse determination of material properties of fin membrane and rays as well as the FSI solver will be presented. A series of validation tests on the material properties and FSI solver will be presented in section 3. In section 4, the integrated model is specified for a juvenile rainbow trout swimming. We demonstrate that it has the capability to accurately predict the hydrodynamic forces and fluid flow in flexible fin propulsion. Finally, this method and the results are briefly summarized in section 5.

2. Numerical approach

2.1. Overview of the integrated approach

A flow chart of our methodology is shown in Fig. 1. The main steps are: (1) reconstructing the geometry and kinematics of the ray-membrane structure of fish fins based on high-speed videos by using an image-based reconstruction method [34]; (2) computing the instantaneous hydrodynamic loading on fin surfaces through CFD simulations by using the reconstructed kinematics as prescribed motion; (3) inversely determining the Young's modulus of each individual fin ray and membrane

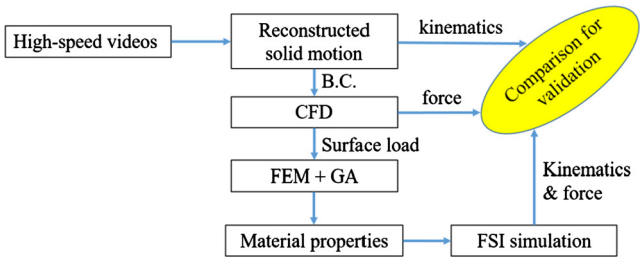

Fig. 1. Flow chart of the integrated methodology.

by combining a FEM model and the genetic algorithm (GA) based optimization; (4) validating the Young's modulus profile through FSI simulations by comparing the kinematics and force with those obtained in the reconstructed model. In the following context, Sections 2.2 and 2.3 will provide more details about the algorithms for the FEM, GA and FSI, and section 4.1 will demonstrate an example of applying the method to obtain the stiffness profile of a caudal fin of a rainbow trout.

2.2. Inverse determination of the material properties

We use finite element (FE) models to model the solid structure in the FSI problem. Generally, input in three categories are needed to build the FE model: (1) the geometrical and structural characteristics; (2) the material properties of the structural components; and (3) the driving kinematics as boundary conditions. Among the three, the geometry and structural characteristics are usually easy to measure; the driving kinematics can be extracted from the video reconstruction. Thus, the only unknown component is the material properties, which are difficult to measure with high accuracy, especially when they are not uniform through the structure. However, since we can obtain the kinematic deformation from the reconstructed kinematics and the surface loading from CFD simulation with the prescribed kinematics, the determination of the material properties poses an inverse problem to the typical FE analysis where the deformation is the unknown.

The genetic algorithm (GA) [35–37] together with the FE model is employed for inversely determining the Young's moduli of fin membrane and rays. Let $\boldsymbol{\chi}$ denote the material properties to be determined. A single objective is defined as a function of $\boldsymbol{\chi}$ as

$$\text{objective} = f(\boldsymbol{\chi}) = \sum_{j=1}^{nt} \sum_{i=1}^{np} \left\| d\mathbf{x}_{FE}^{i} - d\mathbf{x}_{target}^{i} \right\|_{j} \tag{1}$$

where np is the total number of nodal points in the FE model, nt is the total number of time samples in the target deformation, and $d\mathbf{x}^i$ is the displacement vector of the ith point. The subscript FE denotes solution computed by the FE code and the subscript target denotes deformation from the reconstructed kinematics. The GA code is set to minimize the objective. In effect, the objective is the summation of point-to-point distances between the FE solution and the target, and it represents the difference in the deformed shape through the sampled period. In equation (1), all the points are treated equally assuming a uniform mesh. Weighting functions can be readily added for non-uniform mesh if desired. Ideally, the objective goes to zero and the material properties are found so that the deformation from the FE model identically matches the target deformation. In cases where the objective doesn't get close enough to zero, the parameter bounds in the GA input need to be adjusted if the optimized results are right at the given bounds. Otherwise, the inverse problem might be ill-posed and the FE model need to be revised. Please note that, unlike other optimization algorithms such as steepest descent and modified Newton method where a set of initial values is explicitly provided, the GA method randomly generates multiple sets of initial values within the prescribed bounds. The convergence of the final results is regarded as independent of the initial values in GA method.

For real-life problems, especially those with a large number of variables, the objective function listed in equation (1) might be too expensive to be practical. For example, in a fish fin case, the target displacement is obtained from the fin motion at a steady periodic state. However, using a dynamic FE simulation, it takes a long time to pass the transient state to reach the periodic state. The computational cost would become unaffordable as hundreds of generations may be needed in the GA optimization. Thus, a computationally cheaper model is required. Noticing that the fin density is close to that of the water, which makes the fluid inertia force much higher than that of the fin inertia force [8,38], we adopted a quasi-static approach by dropping the inertial term of the solid body in the equation of motion. We use the deformed shape of the fin at a time instant (t) as the base model, and then use the deformed shape at the time instant after a small increment ($t + \Delta t$) as the target deformation. In this way, it's assumed that the fin structure is in equilibrium at t, and the difference between the deformation at t and $t + \Delta t$ is due to the incremental hydrodynamic loading and driving boundary kinematics. The objective function for the GA is reduced to

$$\text{objective} = f(\boldsymbol{\chi}) = \sum_{i=1}^{np} \left\| d\mathbf{x}_{FE}^{i} - d\mathbf{x}_{target}^{i} \right\| \tag{2}$$

While this simplification introduces additional errors, it can be justified by the significant improvement in computational efficiency as the evaluation time is vastly reduced from dynamic problems to static problems. As will be shown in section 3.4, the speedup can be up to 25 times with about 10% additional error compared to the objective function (1). The error can be reduced by choosing the initial configuration at an instant where the acceleration is the smallest, for example, at mid-swing for the fish fin.

In the current implementation, the GA code is parallelized, and it calls an in-house FEM package, which is able to deal with the non-linearity of both geometry and material properties, to compute the deformation.

2.3. Flow-structure interaction

The flow field is governed by the incompressible Navier–Stokes equations:

$$\frac{\partial u_i}{\partial x_i} = 0$$
$$\frac{\partial u_i}{\partial t} + \frac{\partial u_i u_j}{\partial x_j} = -\frac{1}{\rho_f}\frac{\partial p}{\partial x_i} + \nu_f \frac{\partial^2 u_i}{\partial x_j \partial x_j} \tag{3}$$

where u_i are velocity components in the three directions, p is pressure, and ρ_f and ν_f are flow density and kinematic viscosity, respectively.

The Navier–Stokes equations are solved with our immersed-boundary-method based flow solver [39,40]. The method is briefly summarized as follows. The equations are discretized in space using a cell-centered collocated (non-staggered) arrangement of the primitive variables u_i and p. The fractional step method of Van Kan [41] is used to integrate the equations in time, which consists of three substeps. In the first substep, a modified momentum equation is solved to get an intermediate velocity u^*. A second-order Adams–Bashforth scheme is employed for the convective terms while the implicit Crank–Nicholson scheme is used to discretize the diffusion terms to eliminate the viscous stability constraint. The second substep requires the solution of the pressure correction equation, which is solved with a highly efficient geometric multigrid method. Once the pressure is obtained, the velocity field is updated to its final value.

The simulation employed a sharp interface immersed boundary method based on a multi-dimensional ghost-cell methodology. The details of the methodology are explained by Mittal et al. [39]. In this method, the solid boundaries are described by triangular elements which are immersed into a Cartesian volume grid. The Cartesian cells are divided into two groups — solid cells and fluid cells, depending on their relative position to the boundary. This ghost-cell method proceeds by first identifying the ghost cells, which are solid cells and each has at least one fluid-cell neighbor. Then a "probe" is drawn from each ghost cell toward the fluid domain to create an image cell. The probe is normal to the boundary and its intersection with the boundary is midway between the ghost node and the image-point. The value of flow variables at the image point is obtained through bilinear interpolations (trilinear in 3D) using values of the surrounding fluid cells. Following this, the value of the variable at the ghost-cell is computed by using a central-difference approximation along the normal probe such that the prescribed boundary condition at the boundary intercept is incorporated. Using this procedure, the boundary conditions are prescribed to the second-order accuracy, and this, along with the second-order accurate discretization of the fluid cells, leads to the local and global second-order accuracy in the computations.

The dynamics of the solid body is simulated using the aforementioned FEM package. This solver is implicitly coupled with the flow solver for FSI simulation. The flow and solid solvers share the triangular mesh on the exposed surface of the solid. The pressure and the shear stress are interpolated from the fluid onto the nodes of the solid surface mesh. A brief summary of the coupling process is as follows:

1. At time level N, iterative step number m, the fluid loading $\mathbf{f}^{N,m}$ is computed through the CFD simulation with the boundary condition of $\mathbf{X}_b^{N,m}$ and $\mathbf{V}_b^{N,m}$, where $\mathbf{X}_b^{N,m}$ and $\mathbf{V}_b^{N,m}$ are the position and the velocity of the solid surface nodes, respectively (when $m=1$, the position is prescribed by $\mathbf{X}_b^{N,1} = \mathbf{X}_b^{N-1} + dt \cdot \mathbf{V}_b^{N-1}$ and the velocity is $\mathbf{V}_b^{N,1} = \mathbf{V}_b^{N-1}$, where $\mathbf{X}_b^{N-1}$ and $\mathbf{V}_b^{N-1}$ is surface position and velocity at time level $N-1$).
2. The solid dynamics with $\mathbf{f}^{N,m}$ held constant is then solved for one full time step and $\mathbf{X}_b^{predicted}$ and $\mathbf{V}_b^{predicted}$ are obtained in the end. This step may be further split into several substeps depending on the stability of the structure solver.
3. The position and velocity of the solid surface for the new iterative step are obtained by the Aitken adaptive under-relaxation scheme to ensure the numerical stability: $\mathbf{X}_b^{N,m+1} = \omega_m \mathbf{X}_b^{predicted} + (1-\omega_m)\mathbf{X}_b^{N,m}$ and $\mathbf{V}_b^{N,m+1} = \omega_m \mathbf{V}_b^{predicted} + (1-\omega_m)\mathbf{V}_b^{N,m}$, where ω_m is the under-relaxation factor.
4. $\mathbf{X}_b^{N,m+1}$ and $\mathbf{V}_b^{N,m+1}$ are supplied to the flow solver and Eq. (3) is solved; velocity and pressure in the flow field is obtained.
5. The hydrodynamic load $\mathbf{f}^{N,m}$ is obtained from the updated flow field, and the procedure is repeated over from step 2 until $|\mathbf{X}_b^{N,m+1} - \mathbf{X}_b^{N,m}| \le \varepsilon$.

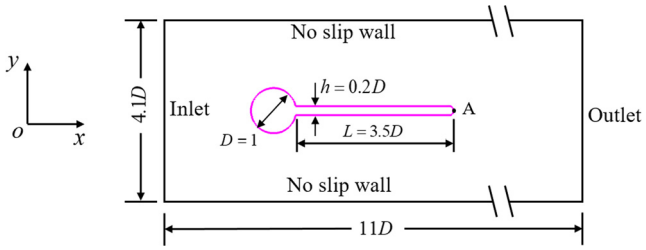

Fig. 2. Schematic and boundary conditions of the 2D validation case.

For the first three iterations of a time level, ω_m in step 3 is fixed as $\omega_m = 0.1$. But when $m > 3$, the under-relaxation factor ω_m is calculated by $\omega_m = 1 - \gamma_m$, where γ_m is the Aitken factor is defined as

$$\gamma_m = \gamma_{m-1} + (\gamma_{m-1} - 1)\frac{(\Delta\delta\mathbf{X}_b^{N,m-1} - \Delta\delta\mathbf{X}_b^{N,m}) \cdot \Delta\delta\mathbf{X}_b^{N,m}}{(\Delta\delta\mathbf{X}_b^{N,m-1} - \Delta\delta\mathbf{X}_b^{N,m})^2},$$

where $\Delta\delta\mathbf{X}_b^{N,m} = \delta\mathbf{X}_b^{N,m-1} - \delta\mathbf{X}_b^{N,m}$ and $\delta\mathbf{X}_b^{N,m}$ is the displacement increment $\delta\mathbf{X}_b^{N,m} = \mathbf{X}_b^{N,m} - \mathbf{X}_b^{N-1}$. Though the computational cost of this implicit coupling is higher compared to an explicit coupling, numerical stability can be achieved through the iteration. Moreover, the iteration ensures that at the end of each time step, the displacement, velocity and the fluid force match between the flow and the solid body.

3. Validation

3.1. FSI validation: flow-induced vibration of an elastic beam behind a cylinder

In this section, a 2D benchmark problem, which is a uniform flow past a flexible beam attached to the downstream side of a rigid cylinder, was first simulated to validate the FSI solver. The problem has been extensively used in past studies as a benchmark case for 2D large-deformation FSI simulation [30,42,43].

The computational domain and boundary conditions are shown in Fig. 2. All the dimensions were normalized by the cylinder diameter, D. The top and bottom sides of the domain were no slip walls. The left side of the domain was the inlet with a parabolic velocity profile along the y-direction [30] and a mean velocity of U. The right side of the domain was the outlet with a Neumann velocity boundary condition. A homogeneous Neumann boundary condition was used for the pressure at all boundaries. The beam thickness and length were $h = 0.2D$ and $L = 3.5D$, respectively. The dimensionless control parameters in the problem were: the dimensionless Young's modulus $E^* = E/\rho_f U^2$, Poisson's ratio ν_s, density ratio ρ_s/ρ_f and the Reynolds number $\mathrm{Re} = UD/\nu_f$, where E and ρ_s are the Young's modulus and density of the solid body, respectively. In this paper, two cases were simulated with: (1) $\rho_s/\rho_f = 10$, $\mathrm{Re} = 100$; (2) $\rho_s/\rho_f = 1$, $\mathrm{Re} = 200$. The values for E^* and ν_s are fixed at 1400 and 0.4, respectively. The simulations were carried out on a non-uniform Cartesian grid with the domain size of $11D \times 4.1D$ and grid number of 256×128 (approximately 32.8 thousand) in total. High-resolution grids (spacing of $0.036D$ and $0.018D$ the x- and y-directions, respectively) were used in the near-body region to resolve the near-field vortex structures. The time step is set to be $dt = 0.005D/U$ to ensure the computational stability.

The time history of the lateral displacement at the beam tip (y coordinate of point A in Fig. 2) for the case with $\rho_s/\rho_f = 10$ and $\mathrm{Re} = 100$ is shown in Fig. 3(a). It shows that at very beginning, the amplitude of beam oscillation is very small. It gradually develops and reaches a periodic state when $\frac{t}{D/U} > 60$, which is consistent with the results of Ref. [43]. The results of Ref. [42,43] during the periodic stage are also included for comparison. During the periodic oscillation, the lateral amplitude of the tip is about $0.95D$ and the oscillation period is about $5.2D/U$. Fig. 3(a) also shows a good agreement between our simulation and those of Ref. [42,43]. Fig. 3(b) shows the vorticity field at a typical time instant, which provides a qualitative comparison of the flow field with that of Ref. [43] (Fig. 2(a) of that paper) and shows a good agreement. The corresponding pressure field at the same moment is shown in Fig. 3(c).

Table 1 summarizes the comparison of tip amplitude A_m/D, Strouhal number St and the drag coefficient with a number of previous studies. The Strouhal number is defined as $St = fD/U$ and the drag coefficient is defined by $C_D = F_x/0.5\rho_f U^2 D$, where F_x is the mean drag of the cylinder-beam system. These quantities show good agreement with previous studies [30, 42,43].

3.2. FSI validation: flow past flexible pitching plates

The FSI solver was further validated through another case which was a uniform flow past a flexible plate in pitching motion [44]. As shown in Fig. 4, a rectangular plate with aspect ratio of $W/L = 0.54$ (W: plate width; L: plate chord length) was put in a uniform flow with an incoming flow speed of U. The position of its leading edge was fixed and the plate was pitching around its leading edge. The pitching angle ($\alpha = \alpha_0 \sin(2\pi f_0 t)$) is prescribed at an amplitude of $\alpha_0 = 12°$.

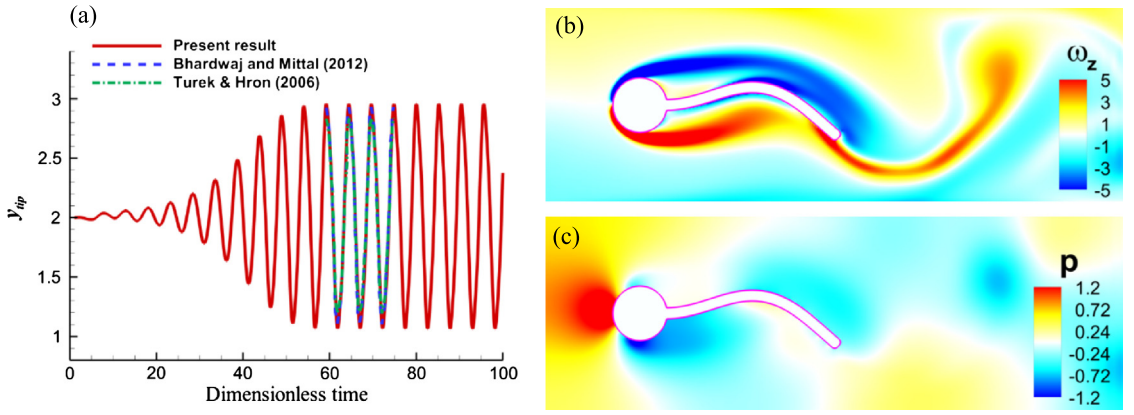

Fig. 3. Results of a 2-D validation case. (a) Time history of the beam tip lateral displacement. (b) Vorticity and (c) pressure field at a typical time instant. The given condition of this case is $\rho_s/\rho_f = 10$, $\mathrm{Re} = 100$, $E^* = 1.4 \times 10^3$ and $\nu_s = 0.4$.

Table 1
Flow-induced vibration of the beam attached to a cylinder: amplitude of the lateral displacement of the beam tip A_m/D, the Strouhal number St, and the drag coefficient C_D.

Cases	Sources	A_m/D	St	C_D
$\rho_s/\rho_f = 10$, $\mathrm{Re} = 100$	Present result	0.95	0.19	4.06
	Turek and Hron [42]	0.83	0.19	4.13
	Bhardwaj and Mittal [43]	0.92	0.19	3.56
	Tian et al. [30]	0.78	0.19	4.11
$\rho_s/\rho_f = 1$, $\mathrm{Re} = 200$	Present result	0.39	0.28	2.26
	Turek and Hron [42]	0.36	0.26	2.30
	Bhardwaj and Mittal [43]	0.41	0.28	2.20
	Tian et al. [30]	0.32	0.29	2.16

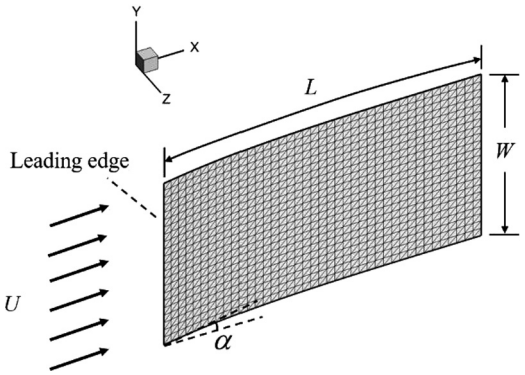

Fig. 4. Flow past a flexible plate which is pitching round its leading edge. $W/L = 0.54$.

The non-dimensional pitching frequency is defined as $f = f_0 L/U$, and is set to be 1 in our simulation. The mass ratio of the plate to the fluid is $\tilde{m} = \rho_s h/\rho_f L = 0.1$, where ρ_s and ρ_f are the plate density and the fluid density, respectively. And h is the plate thickness. The non-dimensional bending stiffness (K) of the plate is defined as $K = EI/\rho_s U^2 L^3$ [44], where E is the Young's modulus of the plate and I is the moment of inertia of the cross section. The plate is discretized by 1760 triangular shell elements. The computational domain size is $10L \times 6L \times 6L$ with $128 \times 64 \times 128$ grid points in total. The minimum grid spacing is $0.025L$ in all x-, y- and z-directions. The time step is chosen as $T/500$, where T is the pitching period.

We simulated a series of cases with bending stiffness K ranging from 0.5 to 50. We plot the normalized trailing edge amplitude (A/L) and the trailing edge phase with respect to the leading edge pitching (ϕ) in Fig. 5(a) and (b), respectively. Results from Dai et al. [44] are superimposed in the figures for comparison purpose. It shows that our results agree well with Dai et al. [44]. We further show the plate profile from the top view for $K = 0.5$ in Fig. 5(c). A similar figure was also shown in Ref. [44]. We found that the simulated plate deformation in this study is identical to that in [44]. The 3D flow field of this case (Fig. 5(d)) also shows the same structures with [44].

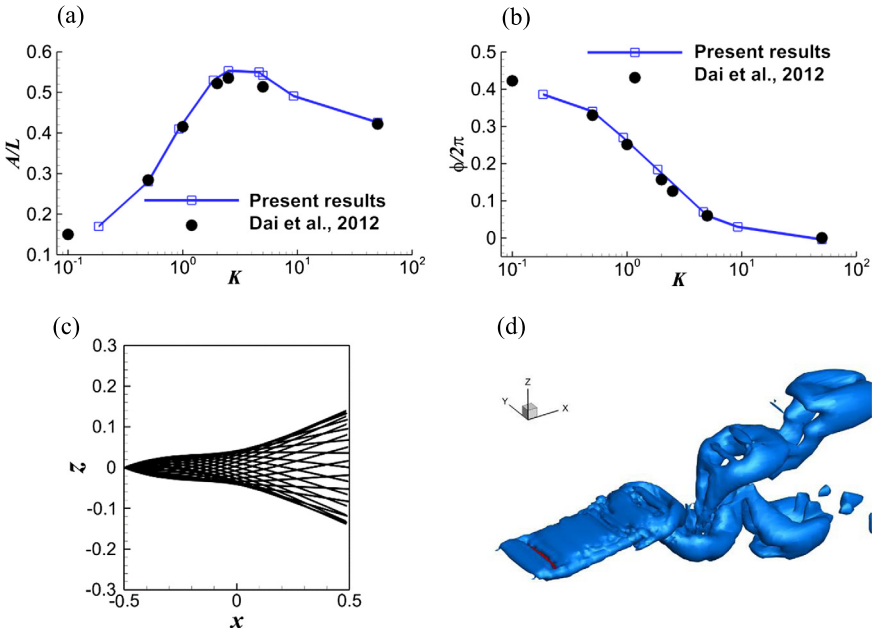

Fig. 5. (a) Trailing edge amplitude of the plate with K. (b) Phase difference between the trailing edge motion and the leading edge pitching with K. (c) Set-up of a flexible plate pitching in free stream. Deformation pattern of the plate with $K = 0.5$, $\alpha_0 = 12^\circ$ and $f = 1$. (d) 3D flow structures of the plate with $K = 0.5$, $\alpha_0 = 12^\circ$ and $f = 1$. For (a) and (b), other parameters in these cases are $\alpha_0 = 12^\circ$ and $f = 1$.

Table 2
GA optimization results for the uniform plate case.

Run no.	E (10^6)	E error%	ν_s	ν_s error%	Objective
1	5.547	−7.6	0.383	53.2	197.3
2	5.81	−3.2	0.311	24.4	123.4
3	5.837	−2.7	0.299	19.6	131.0
4	5.464	−8.9	0.400	60.0	216.0
5	6.111	1.8	0.197	−21.2	100.7
6	5.81	−3.2	0.310	24.0	123.6
average	5.763	−3.9	0.317	26.7	148.7
average2	5.892	−1.8	0.279	11.7	119.7

3.3. GA validation: material properties of a uniform plate

The GA based optimization of the material properties of solid structure in FSI was first validated through one of the previous cases ($K = 0.5$, $\alpha_0 = 12^\circ$ and $f = 1$) in section 3.2. The corresponding Young's modulus and Poisson's ratio are $E/\rho U^2 = 6 \times 10^6$ and $\nu_s = 0.25$, respectively. The GA code was fed with the hydrodynamic load from the FSI simulation. The deformation history of the plate was the target. The same geometrical model and driving kinematics were used. The difference is that now the material properties are the unknowns and need to be determined using GA optimization. For the uniform plate, the material properties are defined by two parameters: the Young's modulus, E, and the Poisson's ratio, ν_s. In this problem, the GA optimization may find the answer within a relatively smaller number of generations considering that only two variables are to be determined. To achieve a higher accuracy, the more expensive objective function defined in equation (1) was used and full dynamic FE simulations were conducted. The optimization was considered to have achieved convergence when the relative change of the objective was less than 1% within 10 consecutive generations. The optimization was run for 6 times when some close answers were found. As we further increased the number of runs, the solution didn't show significant improvement. Similar phenomenon was observed in Ref. [45], in which the results over 30 runs were not better than those of the first 10 runs. The detailed results of this optimization case are listed in Table 2.

For the second average value (average2 in Table 2), the run no. 1 and no. 4 are excluded since the objective is significantly larger than the other cases. The final material properties obtained from the optimization are very close to the actual material properties used in the FSI simulation. The relative error of the Young's modulus is less than 2 percent. While the error for the Poisson's ratio is relatively larger for its effect on the deformation history is found to be small.

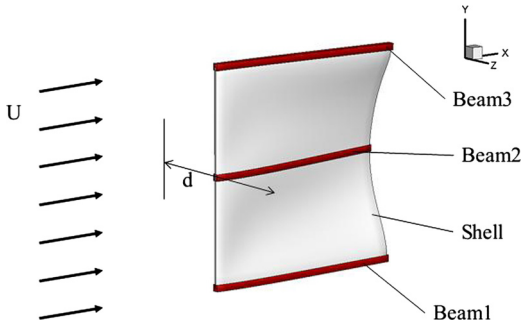

Fig. 6. Hybrid structure of a plate and beams.

Table 3
GA optimization results for the hybrid plate case.

Variable	E_s	E_{b1}	E_{b2}	E_{b3}	ν_s	Residual
Target	1.00E+05	1.00E+08	1.00E+07	5.00E+07	3.00E−01	0
Run1	8.45E+04	1.01E+08	1.05E+07	5.96E+07	3.27E−01	158.9
Run2	9.06E+04	8.96E+07	9.37E+06	4.34E+07	3.80E−01	93.6
Run3	4.20E+04	1.45E+08	1.65E+07	4.34E+07	2.58E−01	201.4
Run4	1.01E+05	9.25E+07	9.50E+06	4.81E+07	2.61E−01	90.1
Run5	9.61E+04	9.43E+07	9.80E+06	4.72E+07	2.84E−01	89.6
Run6	7.05E+04	1.29E+08	1.20E+07	4.81E+07	1.55E−01	123.2
Average of run 2, 4, 5	9.59E+04	9.21E+07	9.56E+06	4.62E+07	3.08E−01	91.1
Error%	−4.10	−7.87	−4.43	−7.53	2.78	

3.4. GA validation: material properties of a hybrid plate

The GA based optimization of material properties was further validated on a hybrid beam-membrane structure. The geometric model is shown in Fig. 6. The model is a square plate reinforced by three beams. It is driven by a heaving motion at the leading edge. Like the previous validation case, the deformation and hydrodynamic loading from FSI simulation were fed to the GA code. The material properties were inversely determined through GA optimization. The extra complexity of this case comes from the number of parameters and the range of the parameters. There are 5 material parameters to be determined: the Young's modulus of the shell (E_s) and three beams (E_{b1}, E_{b2}, E_{b3}), and the Poisson's ratio (ν_s). The range of the moduli spans three orders of magnitude. For the optimization, the parameter bounds of each modulus were specified as an interval spanning three orders of magnitude that contains the target value. The bounds of the Poisson's ratio were [0.15 0.45] with the target value being 0.3. Similar to the previous validation, the objective function (1) was used and we ran the optimization for 6 times. The final averaged answer is given in Table 3. The relative errors for the five parameters are [−4.10%, −7.86%, −4.43%, −7.53%, 2.77%]. The non-uniform distribution of the material properties is captured very well by the GA optimization and the error is within a reasonable range.

To examine the error of the quasi-static assumption, the material properties of this model were also inversely determined using a quasi-static model with the objective function (2). The mid-swing instant was chosen as the initial configuration, and the incremental hydrodynamic loading was computed with a time increment of 1/400 period. The optimization process was also run for 6 times, and the errors are [14.3%, −19.5%, 11.6%, −14.6%, 7.2%]. Comparing the results to those of the dynamic FE simulation, the additional errors are about 5 to 11 percent. While this may seem large, the speedup of the inverse process is about 25 times, which can be the difference between infeasible and practical for non-trivial problems. More importantly, the distribution of the beam stiffness was still captured very well.

4. Application to fish caudal fin propulsion

In this section, we will present the application of the integrated approach to a rainbow trout's caudal fin during propulsion.

4.1. Fish caudal fin kinematic and structural models

A typical fresh water fish often used for analyses of fish propulsion, the rainbow trout (*Oncorhynchus mykiss*), whose caudal fin is its major propulsor, was selected as a representative species for this study. Steady swimming in a flow tank was recorded by a high-speed photogrammetry system from three views (side, back and ventral views, see Fig. 7). The caudal fin kinematics was then reconstructed based on these videos. The reconstruction method is the same as that in studies

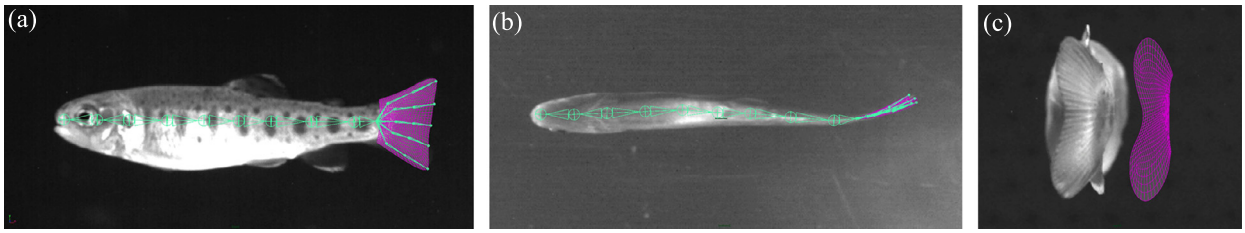

Fig. 7. High-speed images of one individual rainbow trout swimming. (a) Side view; (b) ventral (bottom) view; (c) back view. All three images are synchronized individual frames from high-speed video (500 fps) of steady swimming. In (a) and (b), the virtual skeleton (in cyan) and the caudal model (in purple) is attached to the images to show the reconstruction method. In (c), the reconstructed caudal fin model is shown to compare with the realistic caudal fin shape. (For interpretation of the colors in the figure(s), the reader is referred to the web version of this article.)

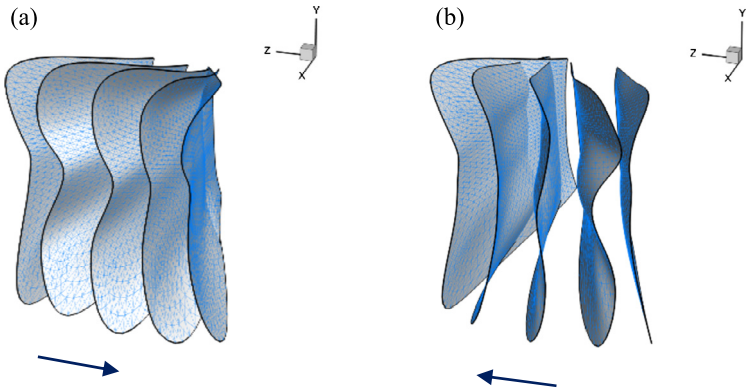

Fig. 8. Reconstructed fin during (a) rightward and (b) leftward flapping. (a) $0 \le t/T \le 0.5$; (b) $0.5 < t/T \le 1$. The arrows indicate the flapping directions.

[24,25,46] and was developed following Koehler et al. [34] for tracking the kinematics of insect flight. For completeness, we briefly summarize this method as follows. The caudal fin was bounded with a series of virtual skeletons, which were connected one after another and can be rotated about their joints with three degrees of freedom (Fig. 7(a), (b)). At each time step, the rotating angles of those skeletons was adjusted to match fin morphing with the high-speed videos. The accuracy of this reconstruction method has been evaluated by comparing the positions of the caudal fin between the model and the high-speed images [34]. The error was found to be less than 5%. Fig. 7(c) shows a comparison between the high-speed image and the reconstructed model in the back view. The reconstructed fin model during the leftward and rightward flapping from the back view is shown in Fig. 8. It shows that the caudal fin exhibits a "W" shape deformation along the spanwise direction. This characteristic is similar to a bluegill sunfish caudal fin during steady swimming [47].

This reconstruction provides us with accurate kinematic data of the caudal fin, which will be used in two ways: (1) as the input for the inverse problem of determining the material properties of fin rays and the fin membrane, and (2) as a reference to validate the FSI solver by comparing predicted to actual kinematics.

The structure of the trout caudal fin is highly non-uniform in both geometry and material composition [13]. The fin is made of pliable material in which bony fin rays are embedded. Each fin ray consists of two half-rays, on left and right side of the fin, separated from each other by a deformable spacer material. In this paper, we are not aiming to include all the details of fin structure. To simplify the problem, we model each fin ray as an integrated beam instead of two separated strips. This simplification was also employed by other previous studies [6–8,20,28]. The structural model of the caudal fin, including the fin rays (in red) and the shell (in gray), is shown in Fig. 9. It has 20 beams in total. The beams are numbered from 1 to 20 from the upper edge to the lower edge. The location and size of these beams are following the same configuration of the rays on a trout caudal fin image [48]. Briefly, the root thickness and the tapering angle are measured by counting pixels on the image. The non-uniform material property of the beams and the shell will be inversely obtained by the GA analysis.

4.2. Hydrodynamic loading on the reconstructed model

A CFD simulation was first carried out to compute the hydrodynamic loading on the fin surfaces at each time instant. The computational domain was $15c \times 10c \times 10c$ (c: fin chord length) with $256 \times 128 \times 256$ (approximately 8.4 million) grid points in total. High-resolution grids (spacing of $0{:}025c$, $0.023c$ and $0{:}021c$ in the x-, y- and z-directions, respectively) were employed round the fin to resolve the near-field vortex structures. Outside the cuboidal region, the grid was stretched to extend to the outer boundary with the same grid spacing gradient in all the six directions. The upstream boundary condition was a constant inflow velocity. The downstream boundary was the outflow boundary, allowing the vortices to convect out of this boundary without reflections. The zero-gradient boundary condition was provided at all lateral boundaries.

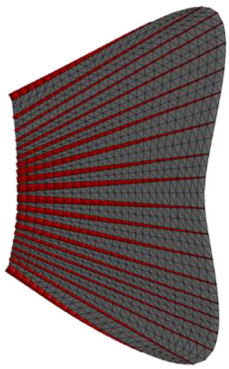

Fig. 9. Structural model of the caudal fin. Fin rays are in red and the shell is in gray.

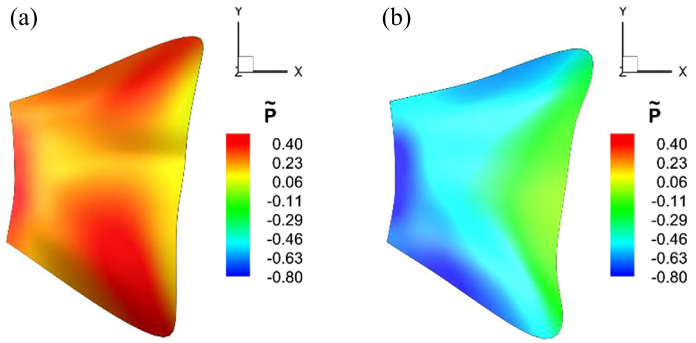

Fig. 10. Distribution of the pressure difference between the right and left sides in the reconstructed model. (a) $t/T = 0.33$; (b) $t/T = 0.87$. (Time period of the leftward flapping: $0 \leq t/T \leq 0.5$ and rightward flapping: $0.5 < t/T \leq 1$.)

A homogeneous Neumann boundary condition was used for the pressure at all boundaries. The Reynolds number (Re) and the Strouhal number (St) was specified based on the experimental measurement. Re based on the chord length is $Re = Uc/\nu = 1000$ and $St = fA/U = 0.44$. Note that in the experiments, a juvenile trout was used with a body length of around 7 cm and the caudal fin chord length of 1 cm.

The major source of the hydrodynamic loading on the surface is the pressure difference between the right and left sides of the fin. Fig. 10(a) and (b) show two snapshots of the pressure difference between the left and right surfaces of a caudal fin at two typical time instants corresponding to the leftward and rightward flapping, respectively. $\tilde{p}$ is the non-dimensional pressure difference between the right and left surfaces, $\tilde{p} = (p_R - p_L)/\rho U^2$. The pressure distribution exhibits both dorsal-ventral and left-right asymmetries, which are because of the asymmetric morphing motion of the fin (will be discussed later). The figures also show that the pressure force is more significant on the region near the dorsal and ventral edges of the fin. This distribution is thought to be associated with the "W" shape deformation of the fin.

4.3. Inversely determined material properties

For the fish fin case, the objective function defined in equation (2) is used since the reconstructed kinematics are only available for the steady periodical motion and the loading history is unknown from the very beginning of the swing. There are 22 parameters in total to be determined using the GA optimization, including the Young's modulus of the fin membrane (shell), the Young's modulus of each fin ray (beams) and the Poisson's ratio which is assumed to be the same for the shell and the beams. The parameter bounds for the moduli are specified as an interval spanning three orders of magnitude that contains reported values obtained from 3-point bending tests [16,49,50]. A population size of 120 was used for this problem. This choice was a balance between the accuracy and computational costs. As a rule of thumb, 5∼10 individuals per variable are considered as a common practice in the application of evolutionary optimization algorithms [51]. Generally, further increasing the population size didn't improve the best answer [45,52].

The final material properties of the beams adopted for further FSI simulation are shown in Fig. 11. The Young's modulus of the beams varies in the range of 0.05∼1.3 GPa, with the edge beams being the stiffest and the center beams next. This is consistent with the material composition of fin rays with the middle and edge rays being the boniest structure. Previous 3-point bending tests on pectoral fins of bluegill sunfish reported Young's modulus in the range of 0.11 GPa to 3.7 GPa [16]. The values of the inversely determined Young's moduli are of the same order of magnitude. The value discrepancy may be due to the different species and the difference between the *in vivo* estimation and the *in vitro* measurement. Fig. 11(b) shows the distribution of the area moment of inertia of the rays. It reflects the thickness variation among the rays and the tapering

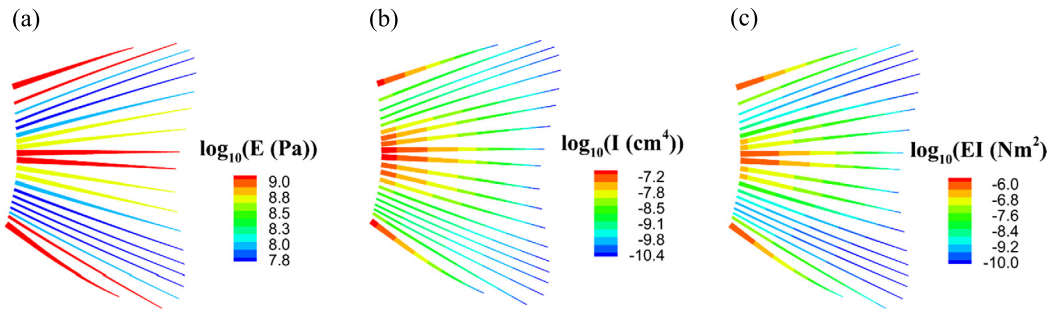

Fig. 11. Inversely determined material properties of the FE fish fin model. (a) Distribution of Young's Modulus E (Pa) among the beams. (b) Distribution of the area moment of inertia I (cm^4) of the beams. (c) Distribution of the flexural rigidity EI (Nm^2) of the beams.

from the root to tip. Combining the area moment of inertia and the Young's modulus, the flexural rigidity of each ray can be computed. Fig. 11(c) shows the distribution of the flexural rigidity of the rays. It is observed that the flexural rigidity is largely determined by the geometrical factor, i.e., the thickness of the beam, which could result in a difference of 3 orders of magnitude in the 2nd moment of cross-sectional area. Due to the tapering of the rays, the flexural rigidity decreases greatly along each ray. Flexural rigidity varying from 4.0e−8 Nm^2 near the distal end to 3.0e−6 Nm^2 near the proximal end can be derived from reported data [16]. The flexural rigidity of current model is of the same order at the proximal end (3.89e−6 Nm^2). But the distal flexural rigidity is much smaller than the reported data. One possible cause is that the caudal fin of the current species has a stronger tapering than the pectoral fin of the reported species. The Young's modulus of the shell among the rays obtained by our GA optimization is about 12 MPa, which is considerably higher than the *in vitro* measurement of the membrane of a bluegill sunfish pectoral fin (0.3∼1 MPa) [53]. But considering the order of magnitude of the Young's modulus of fin rays (GPa), this discrepancy can be neglected. The Poisson's ratio is about 0.4. Again, please note that the cited experimental results are based on the measurement of a bluegill sunfish's pectoral fin, which is different from the current fin and species. To the best of our knowledge, the systematic measurement of the material properties of trout caudal fins are not available at this moment. Thus, it is challenging to directly quantify the error of the fish fin case in the current study.

Based on the results of the fish caudal fin and the validation cases, it is found that the accuracy of the inverse-problem is dependent on the number of the variables. In general, accuracy decreases as the number of variables increases. For example, the relative error of the Young's modulus in a uniform plate with only two variables is less than 2% while it is higher than 4% in a hybrid plate with five variables. Also, the errors of individual variables may be different. The sensitive variables may have a smaller error than those of the non-sensitive variables. For instance, in the validation case of a uniform plate, the relative error of the Young's modulus is less than 2%, while the Poisson's ratio has an error of about 12%. Also, in the inverse problem of the trout caudal fin presented in this section, the Young's moduli of the fin rays are found to have a much smaller relative error than that of the membrane by comparing the GA solutions to the experimental measurements.

As so many parameters need to be determined in this fin fish case, a unique convergence of the solution cannot be always guaranteed given the limited generations and trial runs, but it could be examined by testing it with different swimming kinematics (e.g., at different swimming speeds or different motions) of the same fish. However, such data is not available at this moment.

4.4. FSI simulation and its validation

The obtained Young's moduli were then validated in a fully coupled FSI simulation. In the simulation, the kinematics of the fin root region (within 10% chord) was prescribed through a displacement boundary condition. The fin flapping was driven by the fin root movement, which was a pitching-heaving motion obtained by the reconstruction. The heaving amplitude of the leading edge was about 0.44c. We also found that the trout was actively controlling the pitch angles of the roots of the fin rays. As shown in Fig. 12, the time histories of the roots of the fin rays (beams in structural model, Fig. 12(a)) differ from each other (Fig. 12(b)). The distribution of the pitch amplitude and phase angle exhibit a "U" and a "W" shape respectively. According to these data, the deformation of the fin was initialized by the actuation of the fin root. The movement of the rest of the fin was determined by the flow-structure interactions. We are comparing the deformation pattern, the force production and the flow structures between the FSI case and the prescribed motion case (reconstructed model) in the following.

We show the 3D deformation pattern of the caudal fin obtained by the FSI simulation in Fig. 13. It exhibits similar patterns to that in the reconstructed model shown in Fig. 8. An obvious "W" shape along the spanwise direction can be seen from the back view. To quantitatively compare the flapping kinematics between the FSI model and the reconstructed model, we track three feature points (Fig. 14(a)) on the trailing edge of the fin during a full flapping cycle. The comparison of the lateral displacement (z coordinate) of these points between the two models is shown in Fig. 14(b)–(d). The overall trend of the feature points displacement in FSI model is the same as that in the reconstructed model. Especially, the lateral displacement at point 2, which is at the middle of the trailing edge, showed a high consistency between the FSI

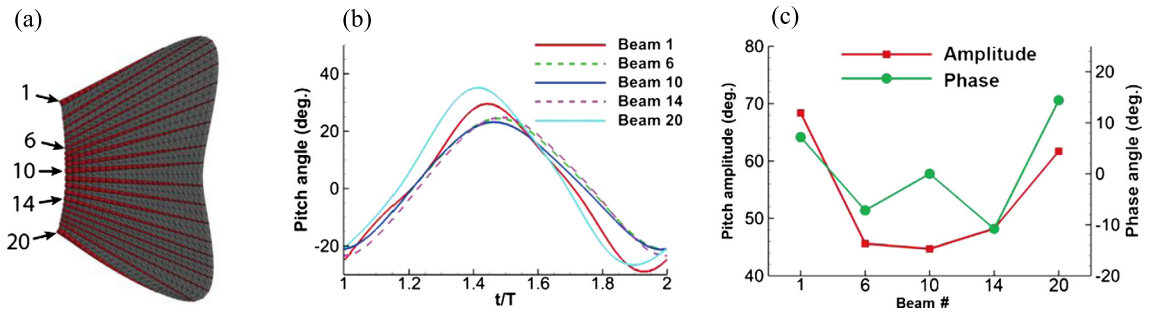

Fig. 12. Pitch angle of the roots of selected fin rays. (a) Number of selected fin rays (beams in the structural model). (b) Time histories of the pitch angle of the select fin rays over a flapping cycle. (c) Pitch amplitude and phase angle of the fin rays.

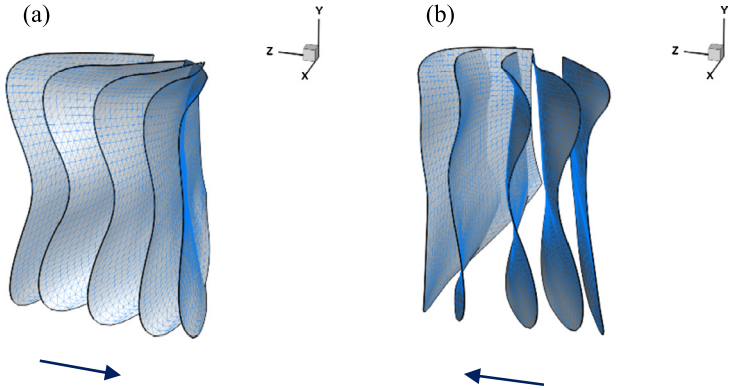

Fig. 13. Caudal fin shape from FSI simulation. (a) Leftward flapping; (b) rightward flapping. $0.5 < t/T \leq 1$. The arrows indicate the flapping directions.

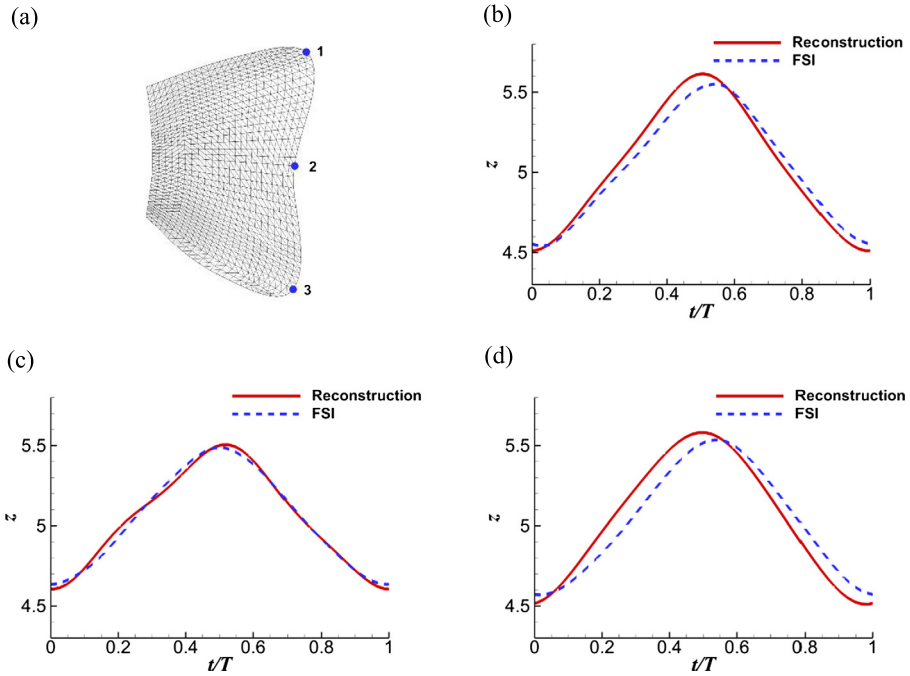

Fig. 14. Three feature points (point 1, 2 and 3) on the trailing edge of the fin model. Lateral displacement of (a) point 1, (b) point 2 and (c) point 3 during a flapping cycle in both the reconstructed model and the FSI model. Peak-to-peak amplitude of point 1 is 1.10c and 1.01c in the reconstruction and FSI, respectively. For point 2, 0.9c in reconstruction while 0.85c in FSI. For point 3, 1.07c in reconstruction while 0.96c in FSI.

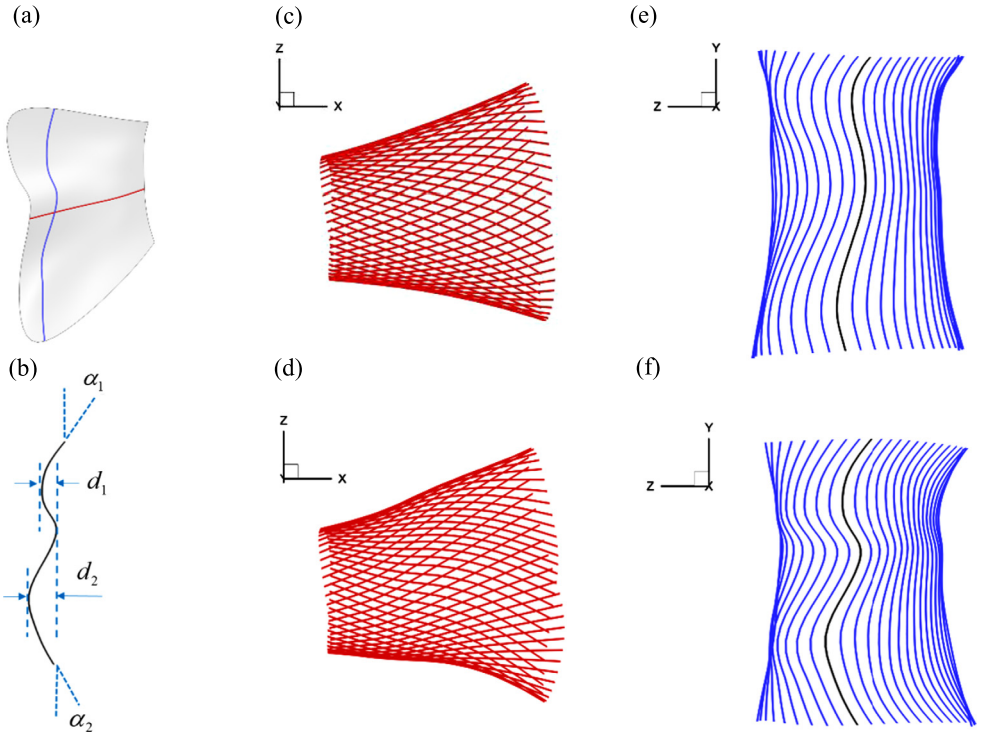

Fig. 15. (a) A horizontal line (in red) at the middle of the fin and a vertical line at 0.8 chord away from the fin root. These two lines demonstrate the chordwise and spanwise deformation, respectively. (b) Measurements of the "W" shape spanwise deformation. Profile of the horizontal lines from the top view in (c) the FSI model and (d) the reconstructed model during a full flapping cycle. Profile of the vertical lines from the back view in (e) the FSI model and (f) the reconstructed model. Only rightward flapping is shown in (e) and (f).

simulation and reconstructed mode. The displacement at point 1 and 3 showed small discrepancy between the two models. The difference of the peak-to-peak amplitude is about 8% and 10% for point 1 and point 3, respectively.

To further compare the details of the fin deformation between the FSI and reconstructed models, we plot the time history of fin profiles at a chordwise location (blue line in Fig. 15(a)) and a spanwise location (red line in Fig. 15(a)) for both models. Fig. 15(c) and (e) are the plots for the FSI simulation. Fig. 15(d) and (f) are the plots for the reconstructed model. It is observed that the deformation profile in the chordwise direction in the FSI model was highly similar to that in the reconstructed model. In particular, the amplitude of mid-chord in the FSI model (Fig. 15(c)) is $0.85c$ and that in the reconstructed model (Fig. 15(d)) is $0.9c$; the difference is less than 6%.

Fig. 15(e) and (f) show that the deformation profile in the spanwise direction in these two models are similar, too. In both models, the fin shows a bell shape with larger amplitudes on the dorsal and ventral edges while a smaller amplitude in the middle region. However, the magnitude of the "W" shape in FSI model appears smaller than that in the reconstructed model. We quantify the "W" shape in Fig. 15(b) by using α_1, α_2, d_1 and d_2, where α is the angle of the upper or lower edge with respect to the vertical direction, and d is the horizontal distance from the convex region to the concave region of the vertical line. The subscripts "1" and "2" correspond to the upper half and the lower half of the vertical line, respectively. We measure α_1, α_2, d_1 and d_2 at midway flapping, as highlighted in black in Fig. 15(e), (f), when the "W" shape is fully developed. It is found that, in the reconstructed model, $\alpha_1 = 41°$, $\alpha_2 = 32°$, $d_1 = 0.086c$ and $d_2 = 0.165c$. In the FSI model, the results are $\alpha_1 = 40°$, $\alpha_2 = 19°$, $d_1 = 0.060c$ and $d_2 = 0.126c$. This difference might be attributed to the integrated effect of the errors introduced by each part of the model, i.e., the reconstruction, structural model and the material property distribution.

Fig. 16 shows the thrust and lateral force coefficients of the FSI model over a flapping cycle along with the results of the reconstructed model. The thrust and lateral force coefficients are defined as $(C_T, C_L) = (F_T, F_L)/0.5\rho_f U^2 S$, where F_T and F_L are the forces in the forward (negative x axis) and lateral (y axis) directions, respectively. S is the area of the fin. From Fig. 16, the time histories of both C_T and C_L of the FSI model are close to those of the reconstructed model. Specifically, the magnitude of thrust peaks of the FSI model is in good agreement with those in the reconstructed model. The time-averaged thrust coefficient $\bar{C}_T$ in FSI model is 0.058, and $\bar{C}_T = 0.042$ in the reconstructed model. Compared with the peak values of the thrust in both cases (around 0.46), the discrepancy ($0.058 - 0.042 = 0.016$) is very small.

Finally, we compare the wake structures between these two models in Fig. 17. Both models show the same flow patterns. There is a vortex ring formed at each half flapping stroke (leftward flapping or rightward flapping). Two sets of vortex rings are therefore formed in the wake. The shape of those vortex rings in both models are identical. Therefore, the flow structures of these two models are in good agreement.

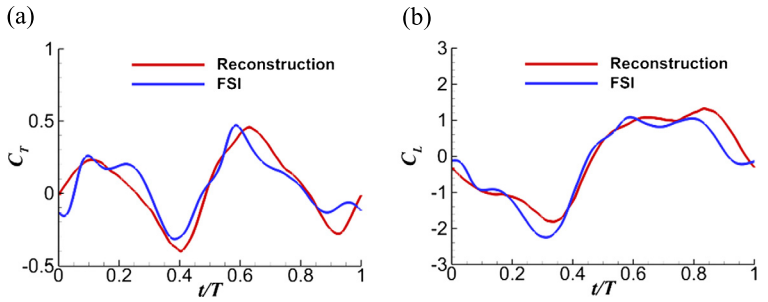

Fig. 16. Comparison of the instantaneous (a) thrust and (b) lateral force coefficients between the FSI model and the reconstructed model.

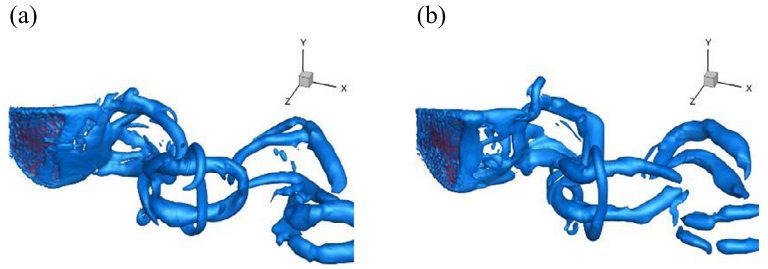

Fig. 17. Isosurface of lambda-2 criterion of the vortical structures at the beginning of leftward flapping of the fin ($t/T = 0.02$) in (a) FSI model and (b) reconstructed model. $|\lambda_2| = 1.2$.

In general, the above comparisons demonstrate that the results of the FSI simulation are consistent with those of the reconstructed model in terms of fin kinematics, force production and the flow structures. But we do observe discrepancies between the results of FSI simulation and reconstructed model. Those discrepancies may be due to the simplifications in our model. In reality, each fin ray is made of two strips (half-rays), showing a bi-laminar structure [13,54]. In addition, fish may actively stiffen each individual fin ray through muscle contraction at the roots of rays which controls the orientation and curvature of rays. Consequently, the internal stress in the rays might be time-varying during fin flapping. This feature would lead to a changing equivalent flexural stiffness over a flapping period [20]. However, the bi-laminar structure and the time variation of stiffness are not considered in our fin ray model for the purpose of model simplification and a lower computational cost. Furthermore, the fish body is not included in our model which may affect the hydrodynamic loading on the caudal fin [24]. Finally, the quasi-static approximation used in the inverse problem may introduce an additional error to the results of the material properties.

5. Summary

In this paper we present an integrated numerical approach for modeling the material properties and the flow-structure interaction (FSI) of flexible solid bodies immersed in flow. Different from traditional FSI modeling, which needs material properties as input *a priori*, the only input of this approach is high-speed video of fin movement. Using an image-based reconstruction method, we build a high-accuracy kinematic model from the high-speed videos first. This kinematic model serves three purposes. (1) It provides the boundary conditions for the CFD solver to obtain surface loading. (2) It provides expected kinematics of the structural model under the loading obtained above, so that the material properties could be correctly determined based on this constraint. (3) It is used as the reference for the validation of the FSI simulation.

The material properties of the solid model are inversely determined by a combined FEM (finite element method) and GA (genetic algorithm) analysis. Supposing the objective function is the sum of the difference of the surface point displacement between the reconstructed model and the FEM model, the solution of the material properties is the one which gives the minimum value of the objective function.

The FSI solver is constructed by coupling of our in-house CFD solver and the FEM package. The CFD solver employs a sharp interface immersed boundary method based on a multi-dimensional ghost-cell methodology. It is able to treat complex and moving boundaries with large deformations. The geometric nonlinearity associated with large deformation is considered in the FEM code. The two solvers share the surface points of the solid body. The solution of FSI is obtained by an implicit coupling which iterates the CFD and FEM solvers. The Aitken under-relaxation scheme is used for the iteration to ensure the computational stability and performance.

The FSI solver is validated by two benchmark cases: flow-induced vibration of a flexible beam attached to a fixed cylinder and a flexible pitching plate in a uniform flow. Our procedure is successfully validated against previous numerical data. The method of inverse determination of material properties is also verified by applying it to the two benchmark cases. Assuming that the material properties are unknown, we find them inversely by the analysis of FEM combined with GA based on the

fluid loading and the kinematics obtained in the FSI simulations. Results show that the inversely determined material properties are very close to those we used in the FSI simulations.

Finally, this approach is applied to a fish caudal fin propulsion problem, which involves complex geometry, large deformation, and multiple unknown material parameters. Following the steps of the integrated method, we reconstruct the caudal fin kinematics based on high-speed videos of a juvenile rainbow trout swimming first. A CFD simulation is then conducted using the reconstructed model as the moving boundary condition. The structural model of the fin is built by considering both the fin rays and the membrane surface. There are in total 22 unknown material parameters. These parameters are inversely determined by the combined FEM-GA method. Finally, a FSI simulation was carried out. And the result of FSI simulation is comprehensively validated on the kinematics, force production and flow structures against the reconstructed model.

Acknowledgements

The authors would like to thank Dr. Valentina Di Santo in the Department of Organismic and Evolutionary Biology at Harvard University for sharing the high-speed videos of trout swimming. Numerical simulations used the Extreme Science and Engineering Discovery Environment (XSEDE) (allocation award number TG-CTS180004).

References

[1] H. Dong, et al., Computational modelling and analysis of the hydrodynamics of a highly deformable fish pectoral fin, J. Fluid Mech. 645 (2010) 345–373.
[2] R. Ramamurti, et al., Fluid dynamics of flapping aquatic flight in the bird wrasse: three-dimensional unsteady computations with fin deformation, J. Exp. Biol. 205 (19) (2002) 2997–3008.
[3] I. Borazjani, M. Daghooghi, The fish tail motion forms an attached leading edge vortex, Proc. R. Soc. Lond. B, Biol. Sci. 280 (1756) (2013) 20122071.
[4] E.G. Drucker, G.V. Lauder, Locomotor function of the dorsal fin in teleost fishes: experimental analysis of wake forces in sunfish, J. Exp. Biol. 204 (17) (2001) 2943–2958.
[5] E. Standen, G. Lauder, Hydrodynamic function of dorsal and anal fins in brook trout (*Salvelinus fontinalis*), J. Exp. Biol. 210 (2) (2007) 325–339.
[6] Q. Zhu, K. Shoele, Propulsion performance of a skeleton-strengthened fin, J. Exp. Biol. 211 (13) (2008) 2087–2100.
[7] K. Shoele, Q. Zhu, Fluid-structure interactions of skeleton-reinforced fins: performance analysis of a paired fin in lift-based propulsion, J. Exp. Biol. 212 (16) (2009) 2679–2690.
[8] Q. Zhu, X. Bi, Effects of stiffness distribution and spanwise deformation on the dynamics of a ray-supported caudal fin, Bioinspir. Biomim. 12 (2) (2017) 026011.
[9] P. Liu, N. Bose, Propulsive performance from oscillating propulsors with spanwise flexibility, Proc. R. Soc. Lond. Ser. A, Math. Phys. Eng. Sci. 453 (1963) (1997) 1763–1770.
[10] P. Prempraneerach, F. Hover, M. Triantafyllou, The effect of chordwise flexibility on the thrust and efficiency of a flapping foil, in: Proc. 13th Int. Symp. on Unmanned Untethered Submersible Technology: Special Session on Bioengineering Research Related to Autonomous Underwater Vehicles, New Hampshire, 2003.
[11] J. Pederzani, H. Haj-Hariri, Numerical analysis of heaving flexible airfoils in a viscous flow, AIAA J. 44 (11) (2006) 2773.
[12] Q. Zhu, Numerical simulation of a flapping foil with chordwise or spanwise flexibility, AIAA J. 45 (10) (2007) 2448–2457.
[13] C. McCutchen, The trout tail fin: a self-cambering hydrofoil, J. Biomech. 3 (3) (1970) 271–281.
[14] B.E. Flammang, et al., Functional morphology of the fin rays of teleost fishes, J. Morphol. 274 (9) (2013) 1044–1059.
[15] G. Lauder, P. Madden, Fish locomotion: kinematics and hydrodynamics of flexible foil-like fins, Exp. Fluids 43 (5) (2007) 641–653.
[16] G. Lauder, et al., Bioinspiration from fish for smart material design and function, Smart Mater. Struct. 20 (9) (2011) 094014.
[17] H. Dong, R. Mittal, F. Najjar, Wake topology and hydrodynamic performance of low-aspect-ratio flapping foils, J. Fluid Mech. 566 (2006) 309–344.
[18] R. Ramamurti, W. Sandberg, Simulation of flow about flapping airfoils using finite element incompressible flow solver, AIAA J. 39 (2) (2001).
[19] H. Dai, H. Luo, J.F. Doyle, Dynamic pitching of an elastic rectangular wing in hovering motion, J. Fluid Mech. 693 (2012) 473–499.
[20] K. Nguyen, et al., Curvature-induced stiffening of a fish fin, J. R. Soc. Interface 14 (130) (2017) 20170247.
[21] P.D. Yeh, A. Alexeev, Effect of aspect ratio in free-swimming plunging flexible plates, Comput. Fluids 124 (2016) 220–225.
[22] R.-N. Hua, L. Zhu, X.-Y. Lu, Locomotion of a flapping flexible plate, Phys. Fluids 25 (12) (2013) 121901.
[23] C. Tang, et al., Self-propulsion of a flapping flexible plate near the ground, Phys. Rev. E 94 (3) (2016) 033113.
[24] G. Liu, et al., Computational analysis of vortex dynamics and performance enhancement due to body-fin and fin-fin interactions in fish-like locomotion, J. Fluid Mech. 829 (2017) 65–88.
[25] F. Fish, et al., Hydrodynamic performance of aquatic flapping: efficiency of underwater flight in the Manta, Aerospace 3 (3) (2016) 20.
[26] Y. Ren, G. Liu, H. Dong, Effect of surface morphing on the wake structure and performance of pitching-rotating plates, in: 53rd AIAA Aerospace Sciences Meeting, American Institute of Aeronautics and Astronautics, 2015.
[27] G. Liu, Y. Yu, B. Tong, A numerical simulation of a fishlike body's self-propelled C-start, in: Recent Progresses in Fluid Dynamics Research: Proceedings of the Sixth International Conference on Fluid Mechanics, AIP Publishing, 2011.
[28] K. Shoele, Q. Zhu, Numerical simulation of a pectoral fin during labriform swimming, J. Exp. Biol. 213 (12) (2010) 2038–2047.
[29] T. Nakata, H. Liu, A fluid-structure interaction model of insect flight with flexible wings, J. Comput. Phys. 231 (4) (2012) 1822–1847.
[30] F. Tian, et al., Fluid–structure interaction involving large deformations: 3D simulations and applications to biological systems, J. Comput. Phys. 258 (2014) 451–469.
[31] M.J. Moulton, et al., An inverse approach to determining myocardial material properties, J. Biomech. 28 (8) (1995) 935–948.
[32] H.-P. Lee, et al., Simulation-based joint estimation of body deformation and elasticity parameters for medical image analysis, IEEE Trans. Med. Imaging 31 (11) (2012) 2156–2168.
[33] S. Yang, M.C. Lin, Material cloning: acquiring elasticity parameters from images for medical applications, IEEE Trans. Vis. Comput. Graph. 22 (9) (2016) 2122–2135.
[34] C. Koehler, et al., 3D reconstruction and analysis of wing deformation in free-flying dragonflies, J. Exp. Biol. 215 (17) (2012) 3018–3027.
[35] D. Goldberg, Genetic algorithms in search, optimization, and machine learning, 1989, IEEJ Trans. Electron. Inform. Syst. 126 (7) (2006) 857–864.
[36] M. Mitchell, An Introduction to Genetic Algorithms, MIT Press, Cambridge, Massachusetts, London, England, 1996.
[37] S. Forrest, Genetic algorithms, ACM Comput. Surv. 28 (1) (1996) 77–80.
[38] C. Brennen, A Review of Added Mass and Fluid Inertial Forces, Brennen (CE), Sierra Madre, CA, 1982.

[39] R. Mittal, et al., A versatile sharp interface immersed boundary method for incompressible flows with complex boundaries, J. Comput. Phys. 227 (10) (2008) 4825–4852.
[40] X. Zheng, et al., A coupled sharp-interface immersed boundary-finite-element method for flow-structure interaction with application to human phonation, J. Biomech. Eng. 132 (11) (2010) 111003.
[41] J. Van Kan, A second-order accurate pressure-correction scheme for viscous incompressible flow, SIAM J. Sci. Stat. Comput. 7 (3) (1986) 870–891.
[42] S. Turek, J. Hron, Proposal for numerical benchmarking of fluid-structure interaction between an elastic object and laminar incompressible flow, in: Fluid-Structure Interaction, Springer, 2006, pp. 371–385.
[43] R. Bhardwaj, R. Mittal, Benchmarking a coupled immersed-boundary-finite-element solver for large-scale flow-induced deformation, AIAA J. 50 (7) (2012) 1638–1642.
[44] H. Dai, et al., Thrust performance of a flexible low-aspect-ratio pitching plate, Phys. Fluids 24 (10) (2012) 101903.
[45] O. Roeva, S. Fidanova, M. Paprzycki, Population size influence on the genetic and ant algorithms performance in case of cultivation process modeling, in: Recent Advances in Computational Optimization, Springer, 2015, pp. 107–120.
[46] G. Liu, et al., Thrust producing mechanisms in ray-inspired underwater vehicle propulsion, Theor. Appl. Mech. Lett. 5 (1) (2015) 54–57.
[47] E.D. Tytell, Median fin function in bluegill sunfish *Lepomis macrochirus*: streamwise vortex structure during steady swimming, J. Exp. Biol. 209 (8) (2006) 1516–1534.
[48] T. Holt, Telling natives from stokies, Available from: https://www.blogflyfish.com/2014/11/telling-natives-from-stockies.html, 2014.
[49] J.M. Horton, A.P. Summers, The material properties of acellular bone in a teleost fish, J. Exp. Biol. 212 (9) (2009) 1413–1420.
[50] S. Alben, P.G. Madden, G.V. Lauder, The mechanics of active fin-shape control in ray-finned fishes, J. R. Soc. Interface 4 (13) (2007) 243–256.
[51] R. Storn, K. Price, Differential evolution – a simple and efficient heuristic for global optimization over continuous spaces, J. Glob. Optim. 11 (4) (1997) 341–359.
[52] T. Chen, et al., A large population size can be unhelpful in evolutionary algorithms, Theor. Comput. Sci. 436 (2012) 54–70.
[53] G.V. Lauder, et al., Locomotion with flexible propulsors: I. Experimental analysis of pectoral fin swimming in sunfish, Bioinspir. Biomim. 1 (4) (2006) S25.
[54] G.V. Lauder, et al., Design and performance of a fish fin-like propulsor for AUVs, in: Proceedings of 14th International Symposium on Unmanned Untethered Submersible Technology, Durham, NH, 2005.